

Statics and dynamics of a cylindrical droplet under an external body force

J. Servantie and M. Müller

Institut für Theoretische Physik, Friedrich-Hund-Platz 1, 37077 Göttingen, Germany

(Dated: October 29, 2018)

We study the rolling and sliding motion of droplets on a corrugated substrate by Molecular Dynamics simulations. Droplets are driven by an external body force (gravity) and we investigate the velocity profile and dissipation mechanisms in the steady state. The cylindrical geometry allows us to consider a large range of droplet sizes. The velocity of small droplets with a large contact angle is dominated by the friction at the substrate and the velocity of the center of mass scales like the square root of the droplet size. For large droplets or small contact angles, however, viscous dissipation of the flow inside the volume of the droplet dictates the center of mass velocity that scales linearly with the size. We derive a simple analytical description predicting the dependence of the center of mass velocity on droplet size and the slip length at the substrate. In the limit of vanishing droplet velocity we quantitatively compare our simulation results to the predictions and good agreement without adjustable parameters is found.

I. INTRODUCTION

Understanding and controlling the motion of droplets is crucial for many practical applications including ink jet printing or microfluidic devices.¹ The motion of droplets can be driven in various ways: For instance, if a temperature gradient is exerted on the fluid the droplet will move because of the Marangoni forces caused by surface tension gradients.² Alternatively, a temperature³ or wettability gradient^{4,5,6} can be applied at the substrate. Forces can also be exerted onto a droplet by immersing it into a sheared, viscous fluid.⁷

Instead of transferring forces via the droplet's surface one can apply a body force. Examples are falling drops on an inclined plane due to gravity^{8,9,10} or the motion of droplets on a rotating disk due to centrifugal forces. In these cases much attention has been devoted to the onset of motion and the changes of the shape of the droplets and their instabilities in response to strong body forces.^{10,11,12,13,14} Surprisingly, the steady-state motion of droplets under these conditions has received little attention.¹⁵ However, this linear regime, where the droplet shape resembles its equilibrium form, is pertinent to small droplets as their occur in nanofluidic devices. In the case of small droplets one can ask the question by which mechanism the energy that is imparted onto the drop via the external force is dissipated. The dominating mechanism is expected to depend on the size of the droplet¹⁶ and it dictates the steady-state velocity of the droplet.

Similar dissipation mechanisms also act when a droplet spreads on a wettable substrate^{17,18,19,20,21,22,23,24} but the study of the steady-state properties is computationally much more convenient because one can average the properties (like the velocity profiles inside the droplet shown in Fig. 1) along the trajectory instead of averaging over many realizations of the spreading process.

Here we study the steady-state of cylindrical droplets under the influence of a weak body force and determine the flow profiles inside of the droplet (see Fig. 1) as well as the relation between the velocity of the droplet's cen-

ter of mass and its size in the linear regime. We derive a simple analytical approximation for the velocity inside the droplet, which is quantitatively compared to the results of extensive Molecular Dynamics simulations of a coarse-grain polymer model.

The manuscript is organized as follows: In Sec. II we describe our simulation model and technique. Then, in Sec. III, we compute properties of the bulk liquid such as surface tension and viscosity. Secs. IV and V comprise the analysis of static properties, such as contact angle and adhesion energy, and dynamics properties of droplets, respectively. The manuscript closes with a brief discussion.

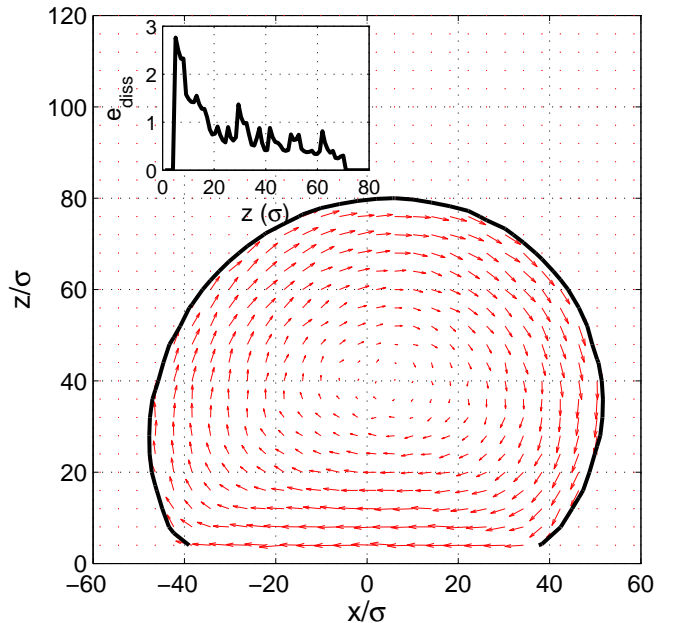


FIG. 1: Velocity field inside a droplet of contact angle $\theta_E = 130^\circ$. The inset represents the viscous energy dissipation per unit volume of fluid as a function of the height.

II. THE MODEL

Being interested in the universal properties of liquid droplets we utilize a coarse-grain model of a polymer liquid.^{25,26,27,28} In experiments as well as simulation studies, polymer liquids are particularly suitable because the vapor pressure is very low and evaporation effects can be disregarded. Moreover, the chain length allows to control the viscosity without changing the molecular interactions. Our coarse-grained polymer model incorporates only the three relevant interactions necessary to bring about the universal properties of dense polymer liquids: connectivity of the segments along the extended macromolecule, excluded volume of the segments on short distances and an attractive interaction at intermediate distances to make the polymers condense into a liquid. Within the framework of such a coarse-grained model, an interaction center – a segment – is comprised of a small number of monomeric repeat units.

Our model for the polymer droplets is similar to the one of Pastorino *et al.* for a polymer melt interacting with a polymer brush.²⁹ The potential between neighboring monomers of a polymer is given by the Finite Extensible Nonlinear Elastic (FENE) potential:

$$U_{\text{FENE}} = \begin{cases} -\frac{1}{2}kR_0^2 \ln \left[1 - \left(\frac{r}{R_0} \right)^2 \right] & \text{for } r < R_0 \\ \infty & \text{for } r \geq R_0 \end{cases} \quad (1)$$

with $R_0 = 1.5 \sigma$ and $k = 30 \epsilon / \sigma^2$. The monomers additionally interact with a 6-12 Lennard-Jones potential,

$$U_{\text{LJ}} = \begin{cases} 4\epsilon \left[\left(\frac{\sigma}{r} \right)^{12} - \left(\frac{\sigma}{r} \right)^6 \right] & \text{for } r < r_c \\ 0 & \text{for } r \geq r_c \end{cases} \quad (2)$$

where the cutoff distance is chosen to be $r_c = 2 \times 2^{1/6} \sigma$. The Lennard-Jones parameters are fixed to unity, $\epsilon = 1$ and $\sigma = 1$. In all the simulation the length of the polymers is fixed to $N_P = 10$ monomers.

The solid, corrugated substrate is modeled by two layers of an fcc lattice of density $\rho_s = 2 \sigma^{-3}$ interacting with the monomers via a Lennard-Jones potential. The length scale of the potential is fixed to $\sigma_s = 0.75 \sigma$, while the strength is varied between $\epsilon_s = 0.2 - 1.0 \epsilon$. The cutoff distance is identical to the range of the interactions in the fluid. This attraction between the polymer segments and the substrate dictates both static properties (e.g., contact angle) and dynamic properties (e.g., slip length).

We use a dissipative particle dynamics (DPD) thermostat in our model. The DPD thermostat has the advantage of acting locally on the system while conserving the momentum. Hence the occurrence of non-physical currents in the fluid is avoided.^{30,31,32} With a DPD thermostat two new force are added to the microcanonical equation of motion,

$$m\ddot{\mathbf{r}}_i = \sum_{j \neq i} (\mathbf{F}_{ij} + \mathbf{F}_{ij}^D + \mathbf{F}_{ij}^R) \quad (3)$$

where m denotes a segment's mass and $\ddot{\mathbf{r}}_i$ its acceleration. \mathbf{F}_{ij}^D and \mathbf{F}_{ij}^R are the dissipative and fluctuating forces acting on particle i due to the interaction with particle j , respectively. In order to conserve momentum these terms are applied to pairs of particles and they take the form:

$$\mathbf{F}_{ij}^D = -\gamma\omega_D(r_{ij}) (\mathbf{1}_{ij} \cdot \mathbf{v}_{ij}) \mathbf{1}_{ij} \quad (4)$$

$$\mathbf{F}_{ij}^R = \zeta\omega_R(r_{ij})\theta_{ij}\mathbf{1}_{ij} \quad (5)$$

where $\mathbf{1}_{ij} = \mathbf{r}_{ij}/r_{ij}$ is the unit vector pointing from particle j to particle i . The damping coefficient, γ , and the strength of the noise, ζ , obey the fluctuation dissipation theorem, $\zeta^2 = 2k_B T \gamma$. We fix $\gamma = 0.5$ in all our simulations. The weight functions are defined as,

$$\omega_R^2 = \omega_D = \begin{cases} (1 - r/r_c)^2 & r < r_c \\ 0 & r \geq r_c \end{cases} \quad (6)$$

and θ_{ij} in Eq. (5) is a random variable of vanishing average and second moment:

$$\langle \theta_{ij} \rangle = 0 \quad (7)$$

$$\langle \theta_{ij}(t)\theta_{kl}(t') \rangle = (\delta_{ij}\delta_{jl} + \delta_{il}\delta_{jk}) \delta(t - t') \quad (8)$$

We use a uniform distribution for θ because it was shown that uniform random numbers give the same results as Gaussian random numbers.³³ The equations of motion are integrated with the velocity Verlet algorithm utilizing a time step $\Delta t = 0.005 \tau$. The temperature is set to $k_B T = 1.2 \epsilon$ in all the simulations. At this temperature the density of the fluid is found to be $\rho_L = 0.788 \sigma^{-3}$ while the vapor density is negligible.^{27,34} Under these conditions, the surface tension is large enough to ensure the stability of droplets under an external force.

III. BULK PROPERTIES

In order to study the statics and dynamics of droplet one needs to evaluate bulk properties of the fluid as a prerequisite. Quantities, such as surface tension and shear viscosity, determine the shape of the droplet and the energy dissipation rate, respectively. First, we compute the self-diffusion coefficient D of the polymers. The system we use in order to do that is a cubic box of size $L = 19.04 \sigma$ containing $N = 5440$ monomers. The diffusion coefficient of a polymer is computed from the integral of the auto-correlation function of the velocity of its center of mass,

$$D = \frac{1}{3} \int_0^\infty dt \langle \mathbf{v}_{\text{CM}}(t) \cdot \mathbf{v}_{\text{CM}}(0) \rangle \quad (9)$$

We find a self-diffusion coefficient $D = 0.0157 \pm 0.0030 \sigma^2 / \tau$. Moreover, computing the end-to-end distance of a polymer we obtain $R_{ee} = \sqrt{\langle R_{ee}^2 \rangle} = 3.447 \sigma$.

The Rouse relaxation time of the polymer is $\tau_P = R_{ee}^2/(3\pi^2 D) = 25.6 \pm 5 \tau$.³⁵ This relaxation time permits to estimate an upper limit of the shear rate that one can apply to the fluid before the polymers starts to be significantly deformed: The Weissenberg number $We = \dot{\gamma}\tau_P$ should be of the order of unity or less, hence $\dot{\gamma}_{\max} \approx 0.05 / \tau$.

The shear viscosity, η , is obtained from the auto-correlation function of the off-diagonal elements of the microscopic flux associated to viscosity,³⁶

$$\eta = \frac{1}{k_B T V} \int_0^\infty dt \langle J_{\alpha\beta}(t) J_{\alpha\beta}(0) \rangle \quad (10)$$

where V is the volume of the fluid and the microscopic flux is,

$$J_{\alpha\beta} = \left(\sum_i m v_i^\alpha v_i^\beta + \sum_{i<j} F_{ij}^\alpha r_{ij}^\beta \right) = V P_{\alpha\beta} \quad (11)$$

where $P_{\alpha\beta}$ denotes the pressure tensor. We use the same system parameters as for the calculation of the diffusion coefficient to compute the shear viscosity. Averaging over $2 \cdot 10^5$ time units τ yields the value $\eta = 5.3 \pm 0.1 \sigma^2 / \sqrt{m\epsilon}$.

Finally, we compute the surface tension, γ , using a slab geometry.^{37,38} In this case the surface tension is found from the anisotropy of the pressure tensor according to:

$$\gamma = \frac{1}{2L_y L_z} \left[\langle J_{xx} \rangle - \frac{1}{2} (\langle J_{yy} \rangle + \langle J_{zz} \rangle) \right] \quad (12)$$

where $L_y = L_z = 30 \sigma$ are the lengths of the simulation box in the y and z directions, respectively. Thus, $2L_y L_z$ is the surface area of the fluid. The box size is $L_y = L_z = 30 \sigma$ and $L_x = 100 \sigma$. In order to compute γ we use a larger system than previously, namely $N = 20\,000$ monomers. The value of the surface tension we obtain is $\gamma = 0.5154 \pm 0.0023 \epsilon / \sigma^2$.

IV. STATICS

In this section, we compute the contact angle and adhesion energy of droplets for various strengths of the polymer-substrate interaction, ϵ_s , and system sizes, N . We use periodic boundaries along the y axis and the droplet spans the simulation cell in this direction. As a consequence, the droplets are cylindrical. By virtue of the cylindrical shape, the radius of the droplet increases as $\sim \sqrt{N}$ (instead of $N^{1/3}$ for a cap-shaped drop) and, thus, larger droplets can be studied. The size of the simulation cell along the y axis is fixed to $L_y = 19.93 \sigma$ in all the following simulations. One can characterize the geometry of a cylindrical droplet by two parameters – the equilibrium contact angle, θ_E , and the radius, R . We have schematically depicted a droplet in Fig. 2.

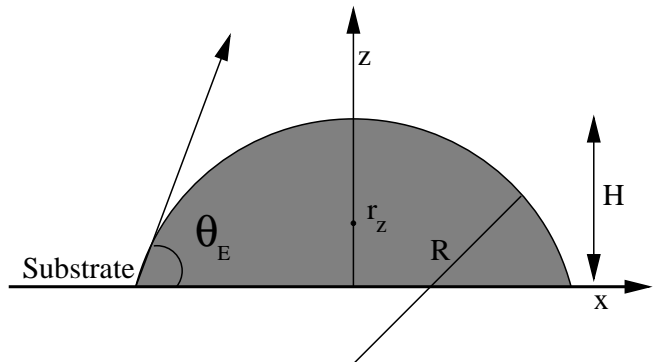


FIG. 2: Sketch of a droplet defining the notations in the text.

Other quantities such as volume V , area A of contact with the substrate, and height of the center of mass r_z can be expressed as a function of R and θ_E . For a cylindrical droplet one obtains the following relations:

$$V = \frac{R^2}{2} (2\theta_E - \sin 2\theta_E) L_y \quad (13)$$

$$A = 2R \sin \theta_E L_y \quad (14)$$

$$r_z = R \left(\frac{4}{3} \frac{\sin^3 \theta_E}{2\theta_E - \sin 2\theta_E} - \cos \theta_E \right) \quad (15)$$

We have computed the equilibrium density profiles for system sizes ranging from $N = 2\,000$ to $N = 100\,000$ monomers and substrate strengths varying between $\epsilon_s = 0.2 \epsilon$ and $\epsilon_s = 0.8 \epsilon$. The statistical average of the density is typically extended over $20\,000$ time units τ and the spatial binning size for the density profiles is chosen as 1σ in both directions. The results are depicted in Figs. 3 and 4.

The contour line represents the average density, $(\rho_L + \rho_V)/2$, between the density of the dense polymer liquid, ρ_L and the vapor, ρ_V which coexists with it. We note that the vapor density is very small ($\sim 10^{-6} \sigma^{-3}$). Utilizing the relation between center of mass height and contact angle (15), one can compute the contact angle in a systematic way without referring to the detailed shape of the liquid-vapor interface in the vicinity of the three-phase contact line. Indeed, one can easily fit a circle to the contours of Figs. 3 and 4 and obtain the curvature, R , of the droplet. On the other hand, the height, r_z , of the center of mass is straightforwardly monitored in the course of the simulation. We depict in Fig. 5 the dependence of the radius on the number of monomers, N , and the height of the center of mass, r_z , as a function of the radius for both systems. As we see, r_z linearly increases with R showing that there is no significant dependence of the contact angle on size. First, the length of the three-phase contact line is independent of the droplet size for a cylindrical droplet.^{39,40} Second, the interface potential, which describes the interaction between the liquid-vapor interface and the substrate, is rather short-ranged. Third, by virtue of the low temperature and the concomi-

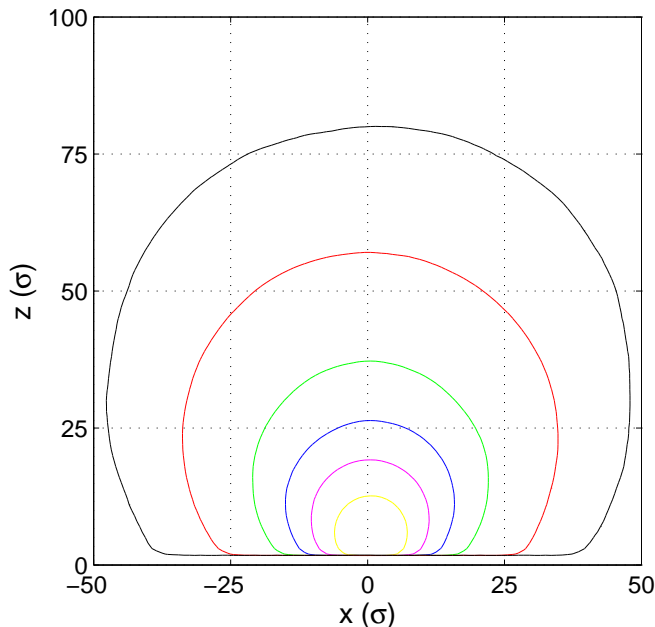


FIG. 3: Density contours for increasing system sizes varying from $N = 2000$ to $N = 100000$ monomers for $\epsilon_s = 0.4 \epsilon$. The equilibrium contact angle is $\theta_E = 130^\circ$.

tantly low vapor density and low liquid compressibility, the shift of the pressure away from the bulk coexistence value due to the Laplace pressure of the curved liquid-vapor interface of the droplet does not give rise to a noticeable change of the liquid or vapor properties.

The slopes of Figs. 5(b) and 5(d) yield the equilibrium contact angles $\theta_E = 130^\circ$ and $\theta_E = 29.4^\circ$ for $\epsilon_s = 0.8\epsilon$ and $\epsilon_s = 0.4\epsilon$, respectively.

We observe that r_z does not vanish for zero radius for two reasons: First, the second layer of the substrate is approximately located at a height of 0.7σ . Second, there is a depletion layer of the polymer liquid near the substrate that shifts the height of the center of mass farther upwards. We applied this systematic method to other substrate strengths in order to evaluate how the contact angle and the adhesion free energy depends on ϵ_s . In equilibrium the macroscopic contact angle of a droplet point is determined by the Young equation,^{41,42}

$$\gamma_{SV} - \gamma_{SL} - \gamma \cos \theta_E = 0 \quad (16)$$

where γ_{SV} , γ_{SL} denote the surface energies between the substrate and the vapor phase, and the substrate and the liquid phase, respectively. One can rewrite Eq. (16) in terms of the adhesion free energy per area unit W as,

$$W = \gamma (1 + \cos \theta_E). \quad (17)$$

As a consequence, the fluid will completely wet the surface if $W \geq 2\gamma$. When $W < 2\gamma$, however, there will be only partial wetting, i.e., droplets with a finite contact

angle will form. Hence, by representing W as a function of the strength of the substrate, ϵ_s , one can extrapolate towards the value where the wetting transition occurs.

Alternatively, one can compute the adhesion energy from the Molecular Dynamics simulations by computing the average energy of the polymer-substrate interactions, $\langle U_{LJ}^s \rangle$. Utilizing the statistical mechanics definition of the free energy

$$F = -k_B T \ln Z \quad \text{where } Z = \int d\Gamma e^{-\beta \epsilon_s V_s}, \quad (18)$$

denotes the partition function and $U_{LJ}^s = \epsilon_s V_s$ the Lennard-Jones interaction between polymer segments and substrate. We differentiate Eq. (18) with respect to ϵ_s . This procedure yields $\partial F / \partial \epsilon_s = \langle V_0 \rangle = \langle U_{LJ}^s \rangle / \epsilon_s$. Integration gives us the free energy as a function of the strength of the polymer-substrate interaction:

$$F = \int_0^\epsilon d\epsilon' \frac{\langle U_{LJ}^s \rangle}{\epsilon'} + C. \quad (19)$$

where C is an unknown constant of integration. The adhesion energy W is then simply, $W = \frac{F}{A}$, where A is the area of the interface between the fluid and the substrate. We have computed this adhesion energy for values of the strength between $\epsilon_s = 0.2 - 1 \epsilon$. The fluid is confined between two substrates perpendicular to the z direction while periodic boundary conditions are applied along the x and y directions. The system dimensions are $L_x = 19.84 \sigma$ and $L_y = 19.93 \sigma$ while the distance between the substrates varies between $L_z = 19.74 - 20.96 \sigma$ in order to maintain the coexistence density in the fluid sufficiently far away from the substrate (bulk). The system is comprised of $N=5440$ monomers. In Fig. 6 we present the results obtained by both methods.

We see that both methods to compute the adhesion free energy are in rather good agreement. The constant of integration is found to be $C \approx -0.05$. This suggest the presence of a weak first order or possibly second order drying transition for small values of ϵ_s in accord with previous studies of Lennard-Jones monomer fluids^{43,44,45} and polymeric fluids at a higher temperature.^{28,46} The small value of the adhesion energy for small values of ϵ_s allows the droplet to easily detach from the substrate due to thermal fluctuations. If an external body force is applied, driven droplets will be unstable under these conditions. On the other hand, the extrapolation of the data for large values of ϵ_s shows that a wetting transition of first order occurs at a substrate strength of approximately $\epsilon_s^{\text{wet}} = 0.82 \epsilon$.

The fact that W is a non-linear function of the substrate strength, ϵ_s , can be rationalized by writing the total substrate-fluid potential energy in the form

$$U_{\text{TOT}} = \int_0^{r_c} dz \rho(z) U_{\text{wall}}(z). \quad (20)$$

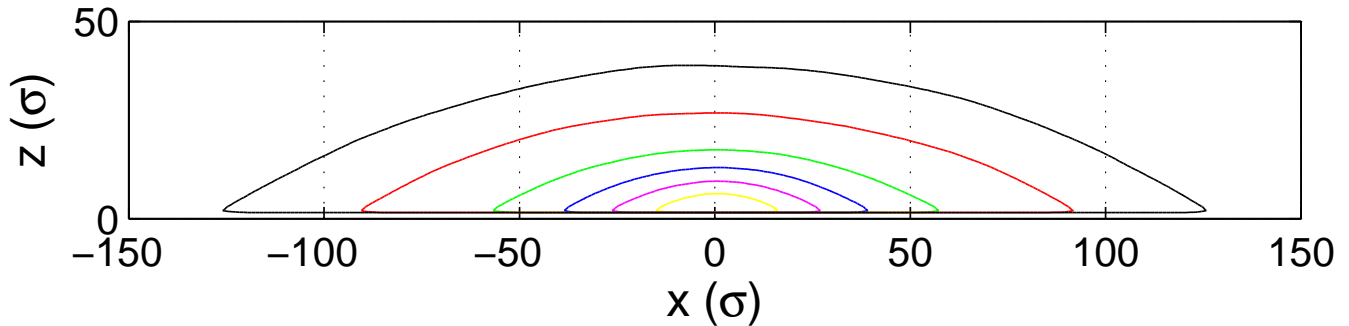


FIG. 4: Density contours for increasing system sizes varying from $N = 2000$ to $N = 100000$ monomers for $\epsilon_s = 0.8 \epsilon$. The equilibrium contact angles is $\theta_E = 29.4^\circ$.

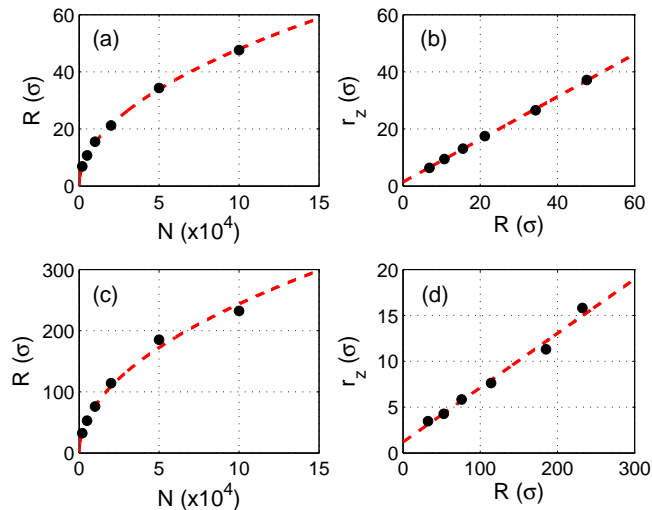


FIG. 5: Radius as a function of the number of monomers and the center mass height as a function of the radius for $\epsilon_s = 0.4 \epsilon$ in respectively (a) and (b), and for $\epsilon_s = 0.8 \epsilon$ in (c) and (d). The circles are the results of the simulations and the dashed line the fits.

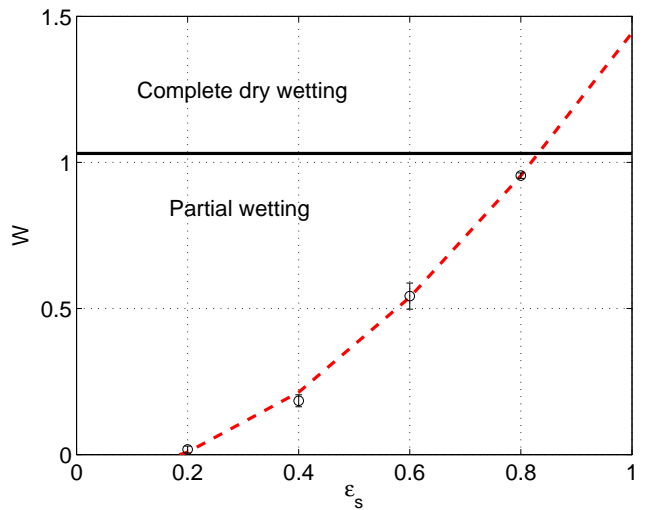


FIG. 6: Adhesion free energy W per area units versus the strength of the substrate ϵ_s . The circles are the data obtained from contact angle computations and with Eq. (17) while the dashed line is from the average Lennard-Jones potential energy according to Eq. (19).

While the substrate potential scales like $U_{\text{wall}} \sim \epsilon_s$, the density also increases with ϵ_s because the wall becomes increasingly attractive giving rise to a strong increase of the adhesion energy and the layering at the substrate.

V. DYNAMICS

A. Boundary condition

When a fluid confined between two walls is sheared with a shear rate $\dot{\gamma}$ a no-slip boundary condition is often observed.^{47,48} However, a finite slippage velocity can occur at non-wetting substrates.^{49,50} The simplest boundary condition that can describe the fluid velocity at the substrate is the Navier slip condition⁵¹

$$\eta \left. \frac{\partial v_x}{\partial z} \right|_{z=z_h} = \lambda v_s \quad (21)$$

that quantifies the balance between the viscous stress due to the shear in the fluid and the friction stress at the boundary. η denotes the viscosity of the liquid, and λ is the friction coefficient. $v_s = v_x(z_h)$ denotes the slip velocity at the hydrodynamic position, z_h of the substrate. The quantity δ

$$\delta = \frac{\eta}{\lambda} \quad (22)$$

characterizes the slip length. If the shear rate $\dot{\gamma}$ is not too large then the slip length, δ , does not depend on $\dot{\gamma}$ and it can be computed by non-equilibrium molecular

dynamics simulation. To this end, one regards the velocity profiles obtained from Couette flow, (i.e., boundary-driven planar shear flow) and Poiseuille flow (i.e., a bulk force is applied to the fluid).

The linear velocity profile of Couette flow,

$$v_x(z) = \frac{v_s}{\delta} [z - z_h - \delta] \quad (23)$$

yields the parameter combination $z_h + \delta$. Additionally, using the velocity profile of Poiseuille flow

$$v_x(z) = \frac{\rho_l a}{\eta} \left[z_h \delta + \frac{1}{2} z_h^2 - \frac{1}{2} z^2 \right] \quad (24)$$

one can compute z_h and δ , independently. Alternatively, one can also evaluate δ from equilibrium molecular dynamics by integrating the auto-correlation function of the tangential force exerted by the wall on the fluid,^{52,53}

$$\lambda = \frac{1}{k_B T A} \int_0^\infty dt \langle F_s(t) F_s(0) \rangle \quad (25)$$

and then the slip length is simply given by Eq. (22) where η is the shear viscosity of the fluid in the vicinity of the substrate. The position z_h of the interface is about σ , which agrees with the shift due to the presence of the substrate. In Fig. 7 we show in the slip length computed by both the non-equilibrium method and the equilibrium one.

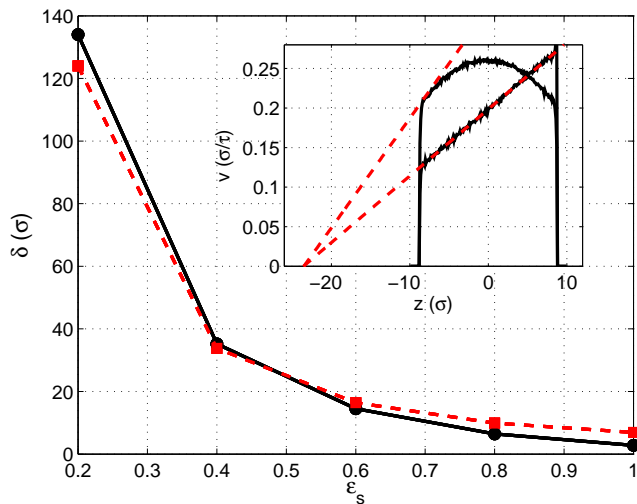


FIG. 7: Slip length δ as a function of the substrate strength ϵ_s . The plain line is obtained from the Couette and Poiseuille profiles while the dashed line from the Green-Kubo relation (25). The inset presents the velocity profiles of the Couette and Poiseuille flow from which the slip length is estimated for $\epsilon_s = 0.6 \epsilon$.

For strong attraction, ϵ_s , between polymer and substrate the Green-Kubo method yields slightly larger values of the slip length than the non-equilibrium method.

This is partially due to the fact that we employ the value of the shear viscosity corresponding to the (bulk) coexistence density, ρ_L , of the liquid, while there are important layering effects present at the substrate for large ϵ_s , enhancing the effective viscosity at the substrate. The largest slip length we observe is smaller than 200 σ compatible with a recent experiment suggesting that slip lengths are of the order of nanometers.⁵⁴

B. Steady state velocity

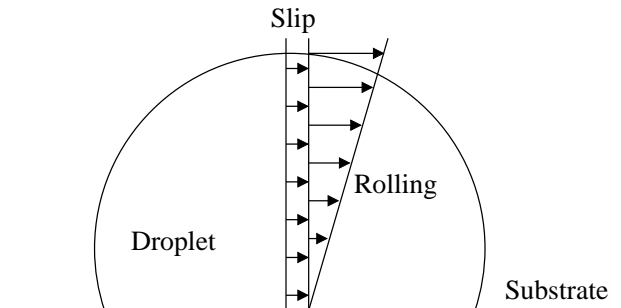


FIG. 8: Sketch of the velocity field inside the droplet.

In order to study the dynamics of the droplet, we apply a constant acceleration a to all particles in the system. After a relaxation time, the droplet attains a steady state where the energy imparted onto the system by the body force is dissipated by the viscous liquid. According to de Gennes⁴² the total energy dissipation rate in the droplet can be decomposed in the following way:

$$T \sum_{\text{TOT}} = T \left(\sum_w + \sum_l + \sum_f \right) \quad (26)$$

where \sum_w is the viscous dissipation due to the rolling motion, \sum_l denotes the dissipation at the three-phase contact line, and \sum_f denotes the dissipation in the precursor film. In our system, the third term can be discarded because there is no precursor film. The second term is due to a possible pinning of the particles of the fluid to the substrate enhancing dissipation at the contact line largely. However, since we use a regularly and finely corrugated substrate in our study one can assume that such processes do not play an important role. Thus, the total dissipation should simply be:

$$T \sum_{\text{TOT}} = T \sum_w \quad (27)$$

However, an extra term should be added to Eq. (27) in case of a finite slip, $\delta > 0$, at the substrate. As sketched in Fig. 8, the velocity field inside the droplet can be decomposed into a rolling motion and the uniform translation with the slippage velocity. This slippage at the

substrate results in a second source of dissipation. Due to the corrugation of the substrate, the fluid in its vicinity undergoes important velocity gradients enhancing the dissipation largely. This description is the microscopic view of the friction between liquid and substrate. Thus, the total dissipation rate can be written as

$$T \sum_{\text{TOT}} = T \left(\sum_w + \sum_A \right), \quad (28)$$

where the term \sum_A is the friction dissipation and it is proportional to the area of contact A between the droplet and the substrate. The second term on the right hand side is exactly known: The power dissipated by the substrate is

$$T \sum_A = F_k v_s \quad (29)$$

where the dynamic friction force F_k is,⁵³

$$F_k = \eta \frac{v_s}{\delta} A \quad (30)$$

If the droplet is sufficiently flat, the dissipation due to the rolling motion can be evaluated in the framework of the lubrication approximation,

$$T \sum_w = \eta \int_V dV \left(\frac{\partial v_x}{\partial z} \right)^2 \quad (31)$$

where V denotes the volume of the droplet. The viscous dissipation scales like the volume V times the square of the shear rate. Thus, for flat droplets, one obtains

$$T \sum_w = \xi \eta \left(\frac{v_s}{\delta} \right)^2 V \quad (32)$$

where ξ is a numerical factor that describes the flow profile inside the droplet and that only depends on the contact angle. Here, we assume that the shear at the substrate $\frac{\partial v_x}{\partial z}|_{z=z_h} = v_s/\delta$ sets the scale of the shear inside the entire droplet. This assumption is obviously fulfilled for droplets with a small contact angle and a large slip length. We will explain below that this viscous volume dissipation is most important for flat drops. Moreover, we shall verify below that this crude assumption remains a reasonably good description even for droplets with a larger contact angle (cf. Fig. 9).

Now, using the fact that the total energy dissipation rate of the system is simply the velocity of the center of mass times the bulk force, one arrives at

$$\rho_L V a U = \eta \frac{v_s^2}{\delta} A + \xi \eta \left(\frac{v_s}{\delta} \right)^2 V \quad (33)$$

$$\approx \eta \left(\frac{U}{\delta + r_z} \right)^2 (\delta A + \xi V) \quad (34)$$

where, in the last step, we have approximated the scale of the typical shear inside the droplet by $U/(\delta + r_z)$.

Eq. (33) describes the cross-over between two regimes: For small drops, $\delta A \gg V$ or $\delta \gg r_z$, the friction at the substrate is the dominant dissipation mechanism. In this limit, we obtain $\eta U/\rho_L a \sim V \delta^2/\delta A \sim R \sim \sqrt{N}$. In the opposite limit, the viscous dissipation inside the droplet dominates and $\eta U/\rho_L a \sim R^2 \sim N$. This phenomenological argument can be generalized to cap-shaped droplets in three dimensions. Then, the rational yields $U/\rho_L a \sim R \sim N^{1/3}$ and $U/\rho_L a \sim R^2 \sim N^{2/3}$ for small and large droplets, respectively.

To turn this phenomenological consideration into a more quantitative description some information about the velocity field inside the droplet is required. The flow inside the droplet is governed by the steady-state Navier-Stokes equation which in the limit of small Reynolds number takes the particularly simple form:

$$\frac{\partial^2 v_x}{\partial z^2} = -\frac{\rho_L a}{\eta} \quad (35)$$

This assumption is justified if the velocity U of the droplet is sufficiently small. Thus, the profile of the velocity v_x parallel to the substrate is a parabolic function of the coordinate, z , perpendicular to the substrate⁴²

$$v_x = \alpha z^2 + \beta z + \gamma \quad (36)$$

We additionally assume that the coefficients, α , β , and γ do not depend on the lateral position, x , inside the drop. From Eq. 35 we read off the first coefficient, $\alpha = -\frac{\rho_L a}{2\eta}$.

Second, we require the tangential stress to vanish at the top of the droplet, i.e., at $z = H$, because the vapor has vanishingly small density and viscosity. By virtue of the symmetry of the (static) droplet profile, the tangential velocity coincides with v_x at the top.

$$\frac{\partial v_x}{\partial z} \Big|_H = 0 \quad (37)$$

This condition determines the coefficient β and one obtains

$$v_x = \frac{\rho_L a}{\eta} \left(H - \frac{z}{2} \right) z + \gamma \quad (38)$$

Finally, we utilize the Navier slip condition (cf. Eq. (21)) at the substrate. In the following we set the origin of the z axis such that $z_h = 0$.

$$v_x(z)|_{z_h=0} = v_s = \gamma = \delta \frac{\partial v_x}{\partial z} \Big|_{z_h=0} = \frac{\rho_L a}{\eta} H \quad (39)$$

This equation determines the slip velocity at the substrate

$$v_s = \frac{\rho_L a}{\eta} H \delta \quad (40)$$

and the velocity profile takes the final form

$$v_x = \frac{\rho_L a}{\eta} \left[\left(H - \frac{z}{2} \right) z + \delta H \right] \quad (41)$$

Eq. (41) provides an approximation of the velocity profile inside the droplet as a function of the droplet shape, the slip length, δ , and the force density $\rho_L a$.

We emphasize that the height appearing in Eq. (41) $H = R(1 - \cos \theta_E)$ does not depend on the lateral position, x . This is in marked contrast to previous work,⁴² where H was chosen as the local height $h(x)$ of the droplet, which characterizes its shape. This identification, however, would result in a spurious singularity of the viscous dissipation at the three-phase contact line.^{55,56} Note that the maximal velocity in x direction, $v_x^{\max} = v_x|_{z=h(x)}$, decreases with the lateral distance from the center of the drop. This behavior implicitly captures some aspects of the rolling motion (cf. Fig. 1).

All parameters that dictate the velocity profile in Eq. (41) have been independently determined: The viscosity η and coexistence density ρ_L are known from the bulk properties of the fluid, the contact angle θ_E from static considerations of droplets and the slip length δ from the Poiseuille and Couette profiles. One can thus predict the velocity profile and quantitatively compare them to the results of the molecular dynamics without any adjustable parameter. This comparison is presented in Fig. 9.

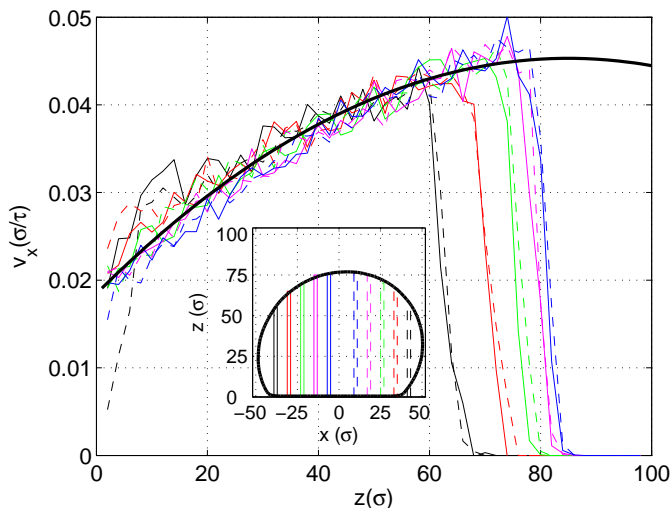


FIG. 9: Velocity profile as a function of the height z for different lateral positions, x , in the droplet. The inset shows the sections which have been used to calculate the velocity profile $v_x(x, z)$.

The comparison validates the basic assumption that the lateral velocity v_x is independent of the lateral position, x . Indeed, the simple analytical expression (41) provides an excellent description of the simulation data using the independently determined parameters.

Considering the velocity at the top of the droplet $v_x = v_x(H)$ one can evaluate the crossover radius R_c between

surface friction and viscous volume dissipation regimes as

$$R_c = \frac{2\delta}{1 - \cos \theta_E} \quad (42)$$

Thus in order to have a large crossover radius, R_c , one should have a large slip length δ and/or a small contact angle, θ_E .

The detailed velocity profile inside the droplet may be difficult to measure experimentally but the cross-over between the two regimes can be observed by the steady-state velocity of the center of mass. Approximating the center of mass velocity simply by the velocity $v_x(r_z)$ at the height of the center of mass r_z , we obtain:

$$U = \frac{\rho_L a}{\eta} \left[\left(H - \frac{r_z}{2} \right) r_z + \delta H \right] \quad (43)$$

In order to test our model we computed the dependence of the steady-state velocity on the droplet size for two substrate strengths, $\epsilon_s = 0.4 \epsilon$ and $\epsilon_s = 0.8 \epsilon$. We first note that our model is valid only for small Reynolds numbers such that no inertial effects are present and the droplet shape resembles its equilibrium shape. Moreover, in this linear regime the center of mass velocity is proportional to the acceleration and, thus, we plot the ratio U/a instead of U .

Care must be taken in choosing the acceleration, a . A too small value of a gives rise to impractically long computation times and large statistical errors in the velocity profiles and the average center of mass velocity. If one chooses a too large, however, non-linear effects become important and one tends to underestimate the ratio U/a . Since at a fixed acceleration, a , the velocity of center of mass increases with size, one reaches the non-linear regime when the droplet size grows. We note that at very high velocities two different behavior can be observed: For small contact angles, the droplets break up into smaller pieces, while for large contact angles they detach from the substrate.

In Fig. 10 and Tab. I we present the results of the simulations and compared them to the predicted behavior (43). We observe that Eq. (43) is in excellent agreement with the results of the Molecular Dynamic simulations. The error bar on the prediction characterize the uncertainty associated with the error of the input parameters. The figure also depicts the asymptotic limits for small and large droplets. Our simulation data are clearly in the cross-over region. The data for the droplet with the larger contact angle (cf. panel a) are mainly in the surface friction dominated regime, while the flatter droplets (shown in panel b) already reach the regime of volume dissipation. The crossover between surface dominated dissipation and volume dominated dissipation occurs at $N_c \approx 160\,000$ and $N_c \approx 33\,000$ monomers for $\epsilon_s = 0.4 \epsilon$ and $\epsilon_s = 0.8 \epsilon$, respectively. Consequently, surface effects are more important than volume dissipation in the

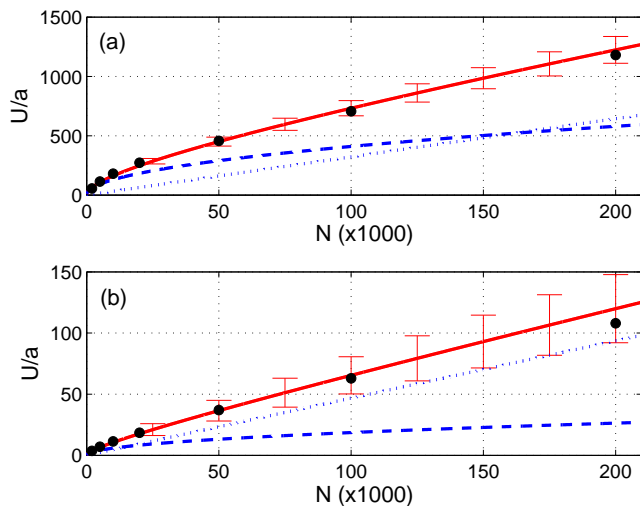


FIG. 10: Velocity of the center of mass per unit acceleration as a function of the number of monomers for (a) $\epsilon_s = 0.4 \epsilon$ and (b) $\epsilon_s = 0.8 \epsilon$. The circles are the results of the molecular dynamics simulations and the dashed lines the analytical results. The error bars mark the uncertainties associated with the independently determined input parameters. The asymptotic limits for small and large droplets are indicated by the solid lines proportional to \sqrt{N} and N , respectively.

ϵ_s/ϵ	N	$U\tau/\sigma$	$a\tau^2/\sigma$
0.4	2000	0.0056	0.0001
0.4	5000	0.0114	0.0001
0.4	10000	0.0180	0.0001
0.4	20000	0.0272	0.0001
0.4	50000	0.0230	0.00005
0.4	100000	0.0364	0.00005
0.4	200000	0.0295	0.000025
0.8	2000	0.000367	0.0001
0.8	5000	0.000699	0.0001
0.8	10000	0.00114	0.0001
0.8	20000	0.00185	0.0001
0.8	50000	0.00185	0.00005
0.8	100000	0.00162	0.000025
0.8	200000	0.0027	0.000025

TABLE I: Parameters and results of the Molecular Dynamics simulations of droplets driven by an external body force.

droplet with the large contact angle. This can be rationalized as follows: In droplets with large contact angles the velocity profile in the upper part of the droplets is close to a purely rotational motion which is characterized by very low dissipation.⁸ This is clearly seen in Fig. 1 which depicts the velocity profile in the comoving frame for a droplet with $N = 100\,000$ monomers and a bulk acceleration $a = 0.00005 \sigma/\tau^2$. Thus, the viscous dissipation in the inside of the droplet is small although the volume is large.

This explanation is corroborated by the profile of the viscous energy dissipated per unit volume of the fluid. In the inset of Fig. 1 we show this quantity as a function

of the height, z . Unfortunately, we are unable to calculate the analog quantity for the droplet with the smaller contact angle with our computational resources because for flat droplets the linear regime is limited to very small accelerations and the velocity of the center of mass is orders of magnitudes smaller than the thermal velocity, $v_T = \sqrt{k_B T/m} = 1.095 \sigma/\tau$.

As we see in the Fig. 1 the energy dissipation rate in a droplet with a large contact angle is twice as large in the lower region than it is in the upper one where the stream lines resemble those of a purely rotational flow. On the other hand, if we decrease the contact angle, the flow inside the droplet will increasingly deviate from this Huygens motion and, consequently the region where important viscous dissipation occurs will expand. As a result, for a small droplet of fixed volume, if the area of contact with the substrate is large (θ_E small) volume dissipation dominates, while if the area of contact is small (θ_E large) surface dissipation dominates.

VI. CONCLUSION

In this paper we studied equilibrium and non-equilibrium properties of polymer droplets in contact with a corrugated substrate by Molecular Dynamics simulations and quantitatively compared the results to a simple analytical model. First, we measured the contact angles for different substrate strength via a geometrical method that does not rely on the detailed shape of the liquid-vapor profile at the three-phase contact line. Additionally, we evaluated the adhesion free energy of the droplet and found good agreement between the shape of the cylindrical droplets and the macroscopic contact angle predicted by the Young equation for our coarse-grain polymer model. In addition to these static characteristics we studied non-equilibrium properties of the system such as the boundary condition (i.e., hydrodynamic interface position and slip length) and the steady-state velocity of the droplet when a bulk force is exerted on it.

An analytical relation predicting the velocity field in the direction of the flow is derived and the scaling of the velocity of the droplet's center of mass discussed. We show that there are two different regime in the droplet dynamics: For small droplets, friction at the substrate dominates dissipation and the droplets velocity, U , increases like \sqrt{N} with the number of particles, N , at constant acceleration. For large droplets, however, the viscous dissipation of the flow in the interior of the droplet dictates the behavior and one observes $U \sim N$. Surprisingly, we find that the larger is the contact angle, and thus the smaller is the area of contact, the larger are the surface effects.

While our study is restricted to cylindrical droplets for computational constraints the qualitative arguments carry over to cap-shaped droplets. The cross-over between the surface- and the volume-dominated dissipation behavior occurs at a droplet radius on the order

$R_c \sim \delta/(1 - \cos\theta_E)$. Using a slip length on the order of micrometer as extracted from recent dewetting experiments by Fetzer *et al.*^{57,58} on low-molecular-weight polystyrene melts on octadecyl- (OTS) and dodecyltrichlorosilane (DTS) polymer brushes and a contact angle of $\Theta_E \approx 67^\circ$ we predict $R_c \approx 3\mu\text{m}$ which is in an experimentally accessible range.

Acknowledgments

The authors thank C. Pastorino for fruitful discussions and the NIC computing center at Jülich for the compu-

tational resources. This research is financially supported by the DFG priority program “nano- and microfluidics” under grant Mu1674/3.

-
- ¹ T. M. Squires and S. R. Quake, *Rev. Mod. Phys.* **77**, 977 (2005).
 - ² M. G. Velarde, *Philos. Trans. R. Soc. London A* **356**, 829 (1998).
 - ³ F. Brochard, *Langmuir* **5**, 432 (1989).
 - ⁴ S.-W. Lee, D. Y. Kwok, and P. E. Laibinis, *Phys. Rev. E* **65**, 051602 (2002).
 - ⁵ F. D. D. Santos and T. Ondarçuhu, *Phys. Rev. Lett.* **75**, 2972 (1995).
 - ⁶ U. Thiele, K. John, and M. Bär, *Phys. Rev. Lett.* **93**, 027802 (2004).
 - ⁷ M. Rauscher, S. Dietrich, and J. Koplik, *Phys. Rev. Lett.* **98**, 224504 (2007).
 - ⁸ L. Mahadevan and Y. Pomeau, *Phys. Fluids* **11**, 2449 (1999).
 - ⁹ U. Thiele, M. G. Velarde, K. Neuffer, M. Bestehorn, and Y. Pomeau, *Phys. Rev. E* **64**, 061601 (2001).
 - ¹⁰ U. Thiele, K. Neuffer, M. Bestehorn, Y. Pomeau, and M. G. Velarde, *Colloids And Surfaces A-Physicochemical And Engineering Aspects* **206**, 87 (2002).
 - ¹¹ H. E. Huppert, *Nature* **300**, 427 (1982).
 - ¹² E. Rio, A. Daerr, B. Andreotti, and L. Limat, *Phys. Rev. Lett.* **94**, 024503 (2005).
 - ¹³ N. L. Grand, A. Daerr, and L. Limat, *Journal Of Fluid Mechanics* **541**, 293 (2005).
 - ¹⁴ N. L. Grand-Piteira, A. Daerr, and L. Limat, *Phys. Rev. Lett.* **96**, 254503 (2006).
 - ¹⁵ H. Y. Kim, H. J. Lee, and B. H. Kang, *Journal Of Colloid And Interface Science* **247**, 372 (2002).
 - ¹⁶ F. Brochard-Wyart and P. G. de Gennes, *Adv. Coll. Interf. Sci.* **39**, 1 (1992).
 - ¹⁷ L. H. Tanner, *Journal Of Physics D-Applied Physics* **12**, 1473 (1979).
 - ¹⁸ M. J. de Ruijter, J. de Coninck, T. D. Blake, A. Clarke, and A. Rankin, *Langmuir* **13**, 7293 (1997).
 - ¹⁹ M. J. de Ruijter, T. D. Blake, and J. de Coninck, *Langmuir* **15**, 7836 (1999).
 - ²⁰ A. Milchev and K. Binder, *J. Chem. Phys.* **116**, 7691 (2002).
 - ²¹ D. R. Heine, G. S. Grest, and E. B. Webb, *Phys. Rev. E* **68**, 061603 (2003).
 - ²² D. R. Heine, G. S. Grest, and E. B. Webb, *Phys. Rev. E* **70**, 011606 (2004).
 - ²³ D. R. Heine, G. S. Grest, and E. B. Webb, *Phys. Rev. Lett.* **95**, 107801 (2005).
 - ²⁴ D. R. Heine, G. S. Grest, and E. B. Webb, *Langmuir* **21**, 7959 (2005).
 - ²⁵ G. S. Grest and K. Kremer, *Phys. Rev. A* **33**, 3628 (1990).
 - ²⁶ C. Bennemann, W. Paul, J. Baschnagel, and K. Binder, *J. Phys.: Condens. Matter* **11**, 2179 (1999).
 - ²⁷ M. Müller and L. G. MacDowell, *Macromolecules* **33**, 3902 (2000).
 - ²⁸ M. Müller, L. G. MacDowell, and A. Yethiraj, *J. Chem. Phys.* **118**, 2929 (2003).
 - ²⁹ C. Pastorino, K. Binder, T. Kreer, and M. Müller, *J. Chem. Phys.* **124**, 064902 (2006).
 - ³⁰ P. J. Hoogerbrugge and J. M. V. A. Koelman, *Europhys. Lett.* **19**, 155 (1992).
 - ³¹ P. Español and P. Warren, *Europhys. Lett.* **30**, 191 (1995).
 - ³² T. Soddemann, B. Dünweg, and K. Kremer, *Phys. Rev. E* **68**, 046702 (2003).
 - ³³ B. Dünweg and W. Paul, *Int. J. Mod. Phys. C* **2**, 817 (1991).
 - ³⁴ L. G. MacDowell, M. Müller, C. Vega, and K. Binder, *J. Chem. Phys.* **113**, 419 (2000).
 - ³⁵ M. Doi and S. F. Edwards, *The Theory of Polymer Dynamics* (Clarendon Press, Oxford, 1996).
 - ³⁶ D. McQuarrie, *Statistical Mechanics* (University Science Books, Sausalito, 2000).
 - ³⁷ M. J. P. Nijmeijer, A. F. Bakker, C. Bruin, and J. H. Sikkenk, *J. Chem. Phys.* **89**, 3789 (1988).
 - ³⁸ P. Orea, Y. Duda, and J. Alejandro, *J. Chem. Phys.* **118**, 5635 (2002).
 - ³⁹ A. I. Hienola, P. M. Winkler, P. E. Wagner, H. Vehkamäki, A. Lauri, I. Napari, and M. Kulmala, *J. Chem. Phys.* **126**, 094705 (2007).
 - ⁴⁰ A. Amirfazli, D. Y. Kwoka, J. Gaydosb, and A. W. Neumann, *J. Colloid Int. Sci.* **205**, 1 (1998).
 - ⁴¹ T. Young, *Philos. Trans. R. Soc. London* **5**, 65 (1805).
 - ⁴² P. G. de Gennes, *Rev. Mod. Phys.* **57**, 827 (1985).
 - ⁴³ P. Adams and J. R. Henderson, *Molecular Physics* **73**, 1383 (1991).
 - ⁴⁴ F. Vanswol and J. R. Henderson, *Phys. Rev. A* **43**, 2932 (1991).
 - ⁴⁵ C. Bruin, M. J. P. Nijmeijer, and R. M. Crevecoeur, *J. Chem. Phys.* **102**, 7622 (1995).
 - ⁴⁶ M. Muller and L. G. Macdowell, *Macromolecules* **33**, 3902 (2000).
 - ⁴⁷ L. Bocquet and J. L. Barrat, *Soft Matter* **3**, 685 (2007).
 - ⁴⁸ E. Lauga, M. P. Brenner, and H. A. Stone, *The no-slip*

- boundary condition, Chapt 15 in Experimental Fluid Dynamics edited by J. Foss, C. Tropea and A. Yarin, cond-mat/0501557* (Springer, Berlin, 2007).
- ⁴⁹ P. A. Thompson and S. M. Troian, *Nature* **389**, 360 (1997).
- ⁵⁰ J.-L. Barrat and L. Bocquet, *Phys. Rev. Lett.* **82**, 4671 (1999).
- ⁵¹ C. L. M. H. Navier, *Mem. Roy. Sci. Inst. France* **6**, 389 (1823).
- ⁵² L. Bocquet and J.-L. Barrat, *Phys. Rev. Lett.* **70**, 2726 (1993).
- ⁵³ L. Bocquet and J.-L. Barrat, *Phys. Rev. E* **49**, 3079 (1994).
- ⁵⁴ L. Joly, C. Ybert, and L. Bocquet, *Phys. Rev. Lett.* **96**, 046101 (2006).
- ⁵⁵ C. Huh and L. E. Scriven, *Journal Of Colloid And Interface Science* **35**, 85 (1971).
- ⁵⁶ E. B. Kim, R. Faller, Q. Yan, N. L. Abbott, and J. J. de Pablo, *J. Chem. Phys.* **117**, 7781 (2002).
- ⁵⁷ R. Fetzer, K. Jacobs, A. Munch, B. Wagner, and T. P. Witelski, *Phys. Rev. Lett.* **95**, 127801 (2005).
- ⁵⁸ R. Fetzer, M. Rauscher, A. Munch, B. A. Wagner, and K. Jacobs, *Europhys. Lett* **75**, 638 (2006).